JOURNAL OF MATERIALS SCIENCE **36** (2001) 1015–1026

Corrosion of TP347H FG stainless steel in a biomass fired PF utility boiler

C. LIU, J. A. LITTLE
Department of Materials Science and Metallurgy, Pembroke Street, Cambridge CB2 3QZ, UK
E-mail: c1120@cus.cam.ac.uk

P. J. HENDERSON, PER LJUNG
Vattenfall AB, Jamtlandsgatan 99, 162 87 Stockholm, Sweden

Detailed microscopic examinations have been conducted on two, temperature-regulated probes which had been exposed to biomass flue gas inside a PF boiler for 3770 h at 600° and 650°C respectively. The two probes were made from commercial grade heat exchanger alloy (TP 347H FG). A significant buildup of potassium chloride and sulphate was found on both probes within the deposits that sinter more strongly on the 650°C probe. Both probes suffer extensive intergranular corrosion as well as general corrosion. The higher temperature enhances scale formation which may provide a beneficial effect with respect to hot corrosion resistance. The intergranular corrosion is linked to the presence of sulphur. The overall material wastage is almost the same for both probes and for different locations covered by deposit.

1. Introduction

There is an increasing interest within the electricity supply industry for more fuel flexibility and the combustion of non-conventional fuels such as waste and biomass instead of coal or oil. This is both to reduce CO_2 emissions and to provide an alternative to dumping of waste. In addition, an improvement in electrical efficiency can be gained by increasing the steam temperature, which leads to more economic fuel utilisation. Burning of biomass causes widespread superheater corrosion, caused by the deposition of alkali chlorides on superheaters with a metal temperature of 500°C or higher. However, most corrosion testing of boiler tubes has been performed in coal-fired environments and, in comparison, relatively little is known about the deposits or corrosion caused by biomass combustion, either at conventional steam temperatures of around 550°C or higher temperatures as anticipated in the future.

At least nine elements are recognised in the literature to contribute to overall deposit chemistry in biomass co-fired boilers [1]: O, Si, Al, Fe, Ca, Na, K, Cl and S, with several others playing minor roles such as Ti, Mg, P and C. They may be present in various chemical forms with silicates, oxides, chlorides, and sulphates being the most common. Alkali metals (K and Na) are known to promote fouling and slagging [2]. Different mechanisms of alkali metal release have also been identified depending on fuel composition and combustion temperature [3], involving potassium/sodium sulphate, chloride, hydroxide or cyanate. Of the multiple stages that occur during biomass combustion, char combustion is the most relevant stage in alkali metal release. Released alkali metals form deposits on cooler surface of furnace components made from alloys, ceramics and refractory materials, causing severe loss in heat transfer efficiency and also materials degradation. The primary processes responsible for deposition have been identified as: inertial impaction, thermophoretic deposition, condensation and chemical reaction. Chlorine released during combustion mainly facilitates the mobility of many species, in particular potassium, and therefore a high concentration of potassium chloride is often found in deposits. Compared to other fuels (e.g., coal), biomass has a higher concentration of alkalis and therefore severe slagging and corrosion problems are expected [4]. Higher levels of silica and, to a lesser extent alumina, are likely to reduce corrosion. The alkali salts becomes "sticky" because of the increasing temperature gradient across the deposits and, as a consequence, more fly ash particles are captured. Thermal dissociation and other reactions of the ash compounds also occur resulting in the formation of low melting point slags once the local concentration reaches the eutectic points [5, 6]. These molten slags are capable of destroying the protective oxide scales commonly formed on commercial heat exchanger alloys through fluxing reactions leading to catastrophic corrosion [7, 8].

As a joint initiative funded by the European Union, collaborative efforts are currently being undertaken to understand the consequence of biomass co-combustion on fouling, slagging and corrosion of commercial heat exchanger alloys. The metallurgical study reported here is a part of the programme. Probe samples have been exposed to biomass flue gas for 3770 h inside a PF boiler operated at Vattenfall AB; two probe sections in the form of tube rings were subsequently selected for examination. The temperatures of the two probes were controlled at 600°C and 650°C respectively to

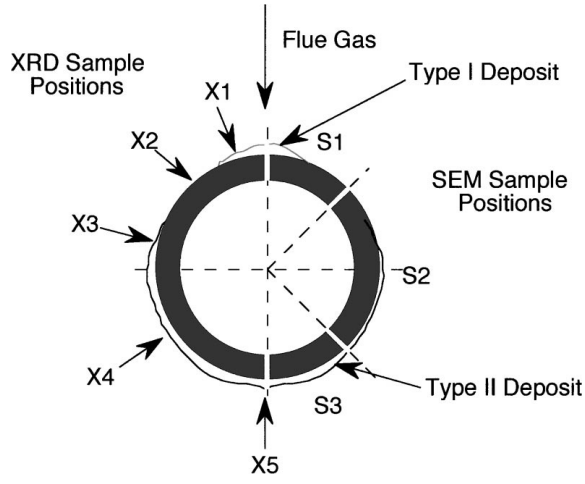

Figure 1 A schematic showing the positions of the two types of deposits on the probes and the positions for subsequent XRD and SEM analysis.

simulate 550 and 600°C steam. The metal surfaces were heated by the flue gases of 800 to 950°C and cooled internally by pressured air. The temperatures were monitored through three thermocouples inserted into the middle (120 degree between them) of the tube wall and were maintained for about 95% of the test period. The tube alloy was commercial grade TP 347H FG stainless steel and Table I lists its compositions. Detailed information about the biomass fuel (a 100% pulverised wood) and its fly ash/flue gas analysis are given in Tables II–IV, respectively. The original probe position inside the flue gas passage is shown in Fig. 1, together with illustrated locations where X-ray diffraction (XRD) and metallographic (optical and electron) samples were taken for examination. XRD measurements were carried out on the probe surface with the deposit attached, whereas the metallographic examinations were mainly on the cross sections of both the tube alloy and the deposit. These locations were chosen to give a representative overview of the material wastage information on the probe.

Corrosion morphologies found on these retrieved corrosion probes (described later) show the characteristics of hot corrosion at relatively low temperature (the so-called Type II hot corrosion) [9, 10]. This is usually attributed to the formation of low melting point complex salts between sulphates from the deposits and metal elements from the alloy [9–12]. The detailed mechanism of this type of hot corrosion remains unclear, even under coal combustion conditions [13]. For Type II hot corrosion under biomass deposits that is usually rich in alkali chlorides, accelerated 'active' oxidation by forming volatile metal chlorides has been proposed to be a possible mechanism [14–16], but this remains to be confirmed by both laboratory studies and industrial trials.

TABLE I Chemical composition (wt%) of TP 347H FG alloy

Elements	C	Si	Mn	P	S	Cr	Ni
Composition	0.09	0.39	1.50	0.024	0.001	18.5	11.95

TABLE III Analysis of the fly ash from the 100% wood fuel

Composition (wt%)	SiO_2	Al_2O_3	CaO	Fe_2O_3	K_2O	MgO	Na_2O	$S_{(ppm)}$	Cl
SCA	14.1	2.9	20.7	2.7	8.1	4.0	1.0	15500	1.7

Other minor elements analysed but not listed: P_2O_5, TiO_2 and MnO_2, as well as those trace elements listed in the fuel analysis (Table II).

TABLE IV Average flue gas analysis

Fuel	HCl (ppm)	SO_2 (ppm)	CO (ppm)	CO_2(%)	O_2(%)	NO (ppm)
SCA	4	10	10	15	5	101

2. Result and discussion

Visually there seems to be two types of deposit: the first type (Type I) has a dark brown colour, similar to the colour of the fly ash. It forms on a narrow region of the probe surface (directly facing the flue gas passage) and is generally thicker (ca. 2 mm at the thickest point, gradually becoming thinner) than the second type. This type (Type II) has a light grey or light brown colour and is relatively uniform in thickness (estimated to be about 0.5–1 mm). It covers about 2/3 of the tube surface. Between the areas covered by the two types of deposits there are two bands (along the axis of the probe) on the probe surface that have very little deposit. The deposits appear to be well sintered on the probe, particularly the Type II deposit. There may be more deposits on the original probes that are less well sintered and therefore lost during handling. There is no obvious difference in either the colour or the thickness of the deposit at the two temperatures by visual inspection. Using optical microscopy, the maximum metal loss measured from the 600°C sample was 77 ± 5 μm and from the 650°C sample it was 88 ± 5 μm. The inner surface of the two probes had a negligible oxidation loss of less than 10 ± 3 μm for both temperatures. Therefore, there seems to be no significant difference between the two probes in terms of material wastage.

2.1. XRD measurement

Results from the two samples are shown in Fig. 2a and b respectively. For the 600°C probe (Fig. 2a), KCl and

TABLE II Analysis of the biomass fuel SCA (heating value of 20.549 MJ kg^{-1})

Composition (wt%)	SiO_2	Al_2O_3	CaO	Fe_2O_3	K_2O	MgO	Na_2O	Ash (%)	C (%)	H (%)	O (%)
SCA	0.0465	0.0103	0.126	0.0119	0.0388	0.0231	0.0172	0.38	47.6	6.1	42.9

Other trace elements (in ppm level): As, Ba, Be, Cd, Co, Cr, Cu, Hg, La, Mo, Nb, Ni, Pb, Sc, Sn, Sr, V, W, Y, Zn, Zr.

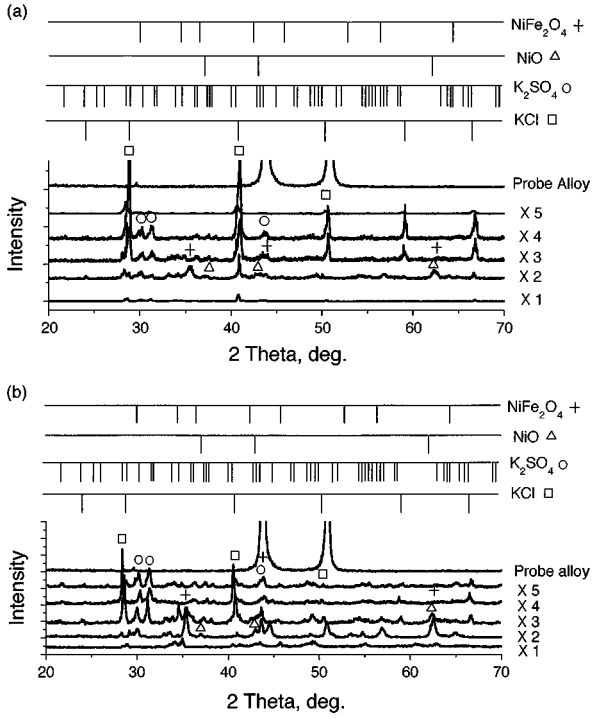

Figure 2 XRD spectra for the 600°C (a) and the 650°C probes (b). For corresponding position of each spectrum, please refer to Fig. 1. The three strongest peaks for each species are also labelled on the spectra.

K_2SO_4 are the two substances clearly detected at almost all locations. As the location changes from X1 to X4, there is a gradual increase of the intensity of the reflection from these compounds and then a decline at location X5. This suggests that a significant proportion of the Type II deposit is made of KCl and K_2SO_4. Another reason for the increased intensity of the reflections is that the deposit at the locations X1 to X4 becomes denser or more crystalline, which may contribute to an enhanced degree of sintering from X1 and X4. Likewise, the spectrum at X1 has lower counts and this may be the result of a loosely sintered deposit. The spectrum from position X2 also has peaks showing the possible presence of NiO and $NiFe_2O_4$. This is expected for X2, as it has almost no deposit (Fig. 1) and hence experiences an environment giving simply oxidation, unlike the other positions. X5 shows low intensities, similar to that of X1, but with slightly stronger KCl peaks. In general, the peak intensity as detected by XRD is a combined result of concentration, crystallinity and surface roughness. The deposit at X5 appears more porous (e.g., than X3 or X4), possibly because it is at the back of the probe, relative to the direction of flue gas, and hence its formation may involve a different deposition mechanism. Other possible, but minor species suggested by XRD include: FeS, FeO(OH), Fe_3O_4, Al_2O_3, $Ca_2V_2O_7$, P_2O_5, Wollastonites ($CaSiO_3$, Ca_3SiO_5, etc.), $CaCO_3$ and K_2CO_3. The percentages of these species in the deposit, if they are detected, are very small. For oxidative corrosion products, iron oxides and NiO (and $NiFe_2O_4$) are detected at the location X2 and possibly exist at other locations as well; chromium oxide is not observed. This however does not imply that chromium oxide is not formed under these conditions (as will be shown later) as chromium oxide and other chromium species are usually formed beneath the iron or nickel oxides, and hence their detection is restricted by the penetration depth of the X-ray source (Cu-K_α penetrates less than 50 μm for polycrystalline materials). Similarly, other reaction products between the deposit and the alloy may also not be detected if they grow deeper into the alloy substrate.

For the 650°C probe (Fig. 2b), the overall trend is quite similar to that observed in Fig. 2a. One clear trend, as compared to the 600°C probe, is that the relative intensity of K_2SO_4 to KCl is increased, indicating a higher concentration of sulphates at higher temperatures, in particular at the locations from X3 to X5. In addition, the peaks for NiO and $NiFe_2O_4$ (possibly Fe_2O_3, $FeCr_2O_4$) are also stronger, which suggests enhanced oxidation. Again there is the same trend of an increase in KCl intensity when the location is changed from X1 to X4 and a further reduction from X4 to X5. The only difference between Fig. 2a and b is that at X5 the dominant species seems to be the sulphate for the 650°C probe rather than KCl as on the 600°C probe.

2.2. Microscopic examination

Typical sections of the probe were cut by hand in order to minimise damage to the deposits. After mounting with a conductive resin, cross sections of the probes were prepared for metallographic examination. Scanning electron microscopy equipped with energy-dispersive X-ray analysis (SEM/EDX) was carried out. Typical results for the 600°C probe are summarised in Fig. 3 on half of the probe. For easier description and comparison of the material lost through corrosion, there characteristic layers are identified in Fig. 3 together with the locations for SEM/EDX analysis. The first characteristic layer (Layer I) forms the outermost scale, which is roughly parallel to the remaining metal surface and may be covered with sintered deposits. The second characteristic layer (Layer II) is the intermediate scale layer, which is often physically separated from Layer I and has the appearance of general corrosion. Unreacted alloy can sometimes be found within this layer. Finally, the third characteristic layer is an internal corrosion layer (Layer III), which has clearly resulted from intergranular corrosion. These features are found to exist for both the 600°C and 650°C probes, although to a different extent.

Detailed micrographs at various locations are shown in Fig. 3a to f. Apart from Fig. 3f (which is from the backside of the probe), the rest of the probe surface suffers a similar extent of corrosion featuring the three characteristic layers. A complete Layer I is not always observed for all of the locations; this is shown in Fig. 3c and 3e where the remaining Layer I seems detached from the underlaying scale. Layer I often appears less dense and mixed with the ash components (Fig. 3c). The dominant corrosion reactions in these environments would be oxidation, hot corrosion by molten deposits (mainly chlorides and sulphates as shown by the XRD measurements), plus possible gas-phase sulphidation and chlorination. The broken and less adherent Layer I therefore offers little barrier to the ingress of either

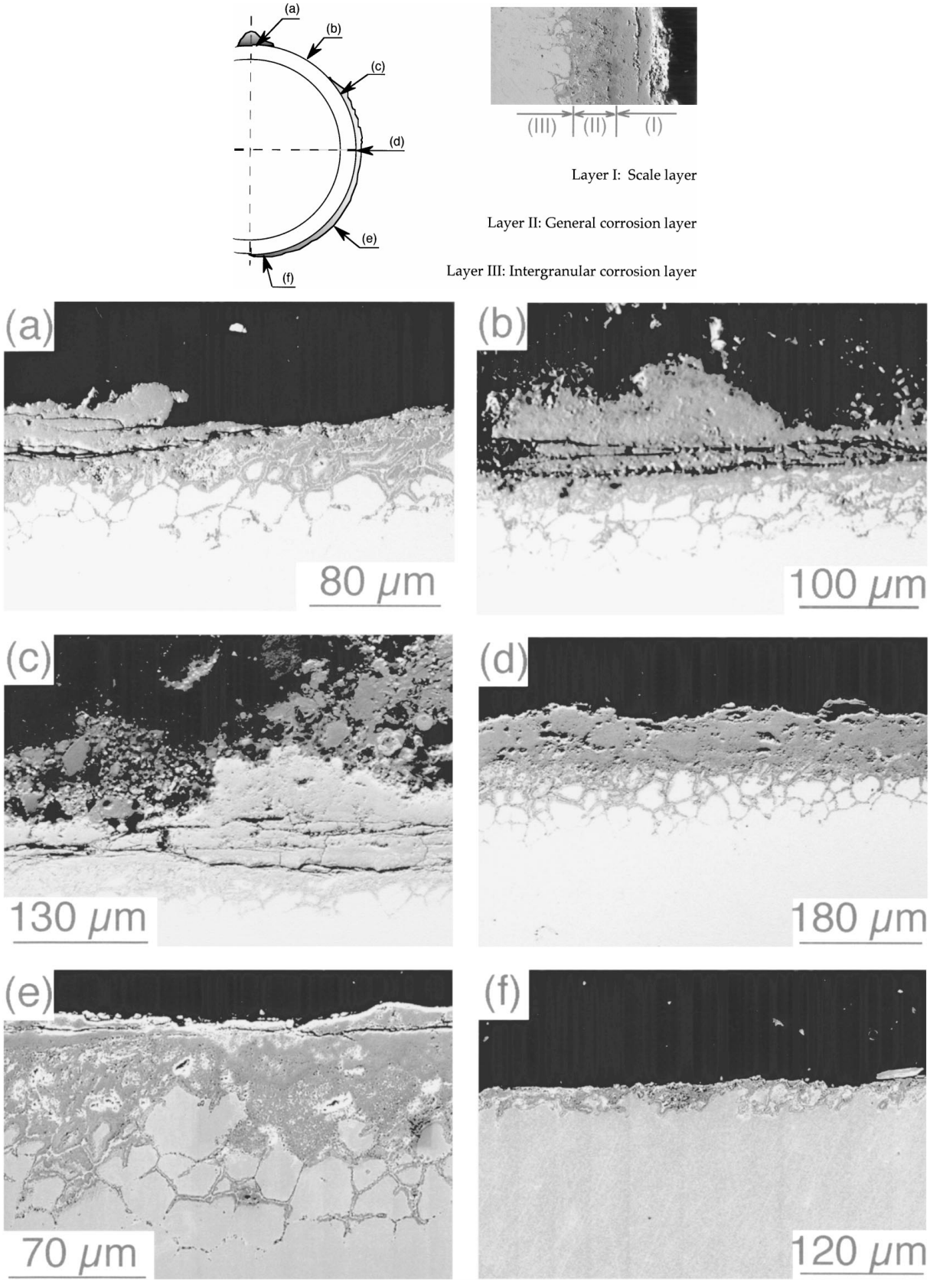

Figure 3 SEM micrographs prepared on the cross sections of the 600°C probe.

gaseous reactants or molten slag towards the remaining tube material. This point may be further illustrated by Fig. 3c: the micrograph shows two regions with the right-side Layer I much thicker than the left-side and this difference appears not to be caused by broken scale on the left-side as both have a thick deposit layer formed on top. It is interesting to note that this large difference in Layer I has apparently very little influence on either the morphology or the thickness of the remaining layers formed beneath (Layers II and III). Despite the care taken during the sample preparation, some loss of deposits is still inevitable with the only micrograph to show extensive deposits being Fig. 3c. The corrosion reaction between the deposits and the metal therefore

bypasses Layer I and continues via grain boundaries and leads to the growth of the other two layers. Completely or partially consumed grains then become Layer II. Fig. 3f is a somewhat exceptional case as it does not seem to follow the classification of three layers. It has no visible scale layer, although it is likely that the original Layer I may have been lost during sample preparation. The major difference is the appearance of the intergranular corrosion layer, which is shallower, wider and also less concentrated at grain boundaries, hence giving an appearance more like pitting. The overall depth of corrosion (without taking into Layer I into account), however, is similar to the other positions.

Fig. 4 shows EDX results across the three characteristic layers (the scale) found at a location close to Fig. 3d (most of the deposit has been lost). As shown in Table V, the clearest trend seems to be the distribution of chromium, which shows a decrease towards the outer surface. This is usually associated with its slow diffusion rate relative to iron and nickel, which leads to an enrichment of chromium at the inner scale and forms the basis for enhanced corrosion protection. Hot corrosion at the grain boundaries, as shown in Fig. 3, is more detrimental, because it penetrates this chromium-rich oxide layer and reduces the possibility of forming a continuous protective layer. Higher iron and nickel contents in Layer I are also evident, although some iron may come from the deposit. The highest sulphur level is at Point 3 and the implication is that sulphur is concentrated in Layer II and its source is the deposit. Despite the high concentration of KCl detected by XRD in Fig. 2a, very little chloride is in fact detected within the scale. This result may be explained by an accelerated "active oxidation" as discussed by Grabke *et al.* [6]: essentially volatile metal chlorides are formed as a result of chlorination and this is followed by re-oxidation on their way to the surface. The chloride level remained within the scale is too low to be detected by EDX, in contrast to the high concentration of KCl in the deposit as detected by XRD. The EDX analysis on the probe alloy itself (Point 4) gives the following results (wt%): 68.3 Fe, 11.6 Ni, 17.7 Cr, 1.7 Mn, 0.59 Si, which is very close to the original composition of the probe alloy (Table I).

TABLE V EDX analysis of the 600°C sample

Elements	Point 1	Point 2	Point 3	Point 4
O	20.1	18.7	11.8	1.0
Fe	63.8	58.6	3.3	68.2
Na	0	0.7	0	0
K	0.3	3.6	0.9	0.2
Ca	0.2	0.4	0.3	0
Mg	0	0.2	0	0.1
Cr	3.9	7.3	37.1	17.8
Mn	5.0	4.9	4.9	1.7
Ni	6.1	4.5	35.4	11.6
Si	0.2	0.1	1.7	0.6
P	0	0	0.1	0.1
S	0.1	0.6	4.0	0.3
Al	0	0.1	0.1	0

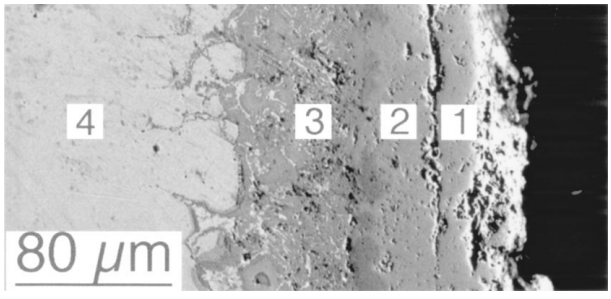

Figure 4 A typical cross section on the 600°C probe and the results of EDX analysis (Table V) carried on the corresponding positions.

An averaged composition analysis as shown in Fig. 4 is less informative when intergranular corrosion has occurred. A more informative analysis is shown in Fig. 5, which is a collection of elemental X-ray maps for the major elements involved in the intergranular corrosion reactions. As shown by Fig. 5, the grain boundaries are generally enriched with chromium and partially with nickel but depleted in iron. The chromium distribution along the grain boundaries is closely matched by oxygen, suggesting the formation of chromium oxides here. More iron can be found in the general corrosion layer, together with nickel. Sulphur is also seen along the grain boundaries, which is closely linked with the nickel distribution, suggesting that the initial corrosion at the grain boundaries involves the formation of nickel-sulphur compounds, possibly Ni_3S_2, NiS or NiS_2. Three characteristic areas are located on the SEM micrograph in Fig. 5, marked by A, B and C, representing different extents of intergranular corrosion. The grain boundary at the area A has a clear band of chromium oxide layer surrounding a nickel and iron centre; the nickel centre is also oxygen deficient but may be enriched with sulphur. Grain boundary corrosion at the location B occupies a much wider area as compared to A and is thus at a more advanced stage of corrosion. Area B has the highest chromium and oxygen intensity and the nickel and iron distribution is relatively isolated and patchy. Similar areas like B can also be identified within Layer II. This possibly represents those areas where there is significant accumulation of chromium together with a high enough oxygen partial pressure to form and maintain a stable chromium oxide. Nevertheless, as shown by the chromium map this chromium oxide layer is far from coherent and uniform. Area C, which corresponds to the designated general corrosion layer, shows a mixture of phases seen in areas A and B. Some are significantly depleted in chromium with rather high concentrations of iron (and oxygen), and others show the opposite. Combined with the EDX results in Fig. 4, it seems that the outer scale layer (Layer I) is mainly iron oxides plus a small quantity of nickel compounds. The general corrosion layer (Layer II) is a mixture of chromium oxide, iron oxide and isolated nickel sulphides and oxide, with clearly segregated boundaries. Finally, the forefront of the intergranular corrosion occurs through oxidation and sulphidation of iron and nickel, leaving chromium to form chromium oxide. The oxide ion concentration is linked to the oxygen partial pressure, which in turn is known to be a function of the SO_2-SO_3 equilibrium that also controls the sulphidation reaction [7]. The chlorine map gives a uniform distribution across the region and

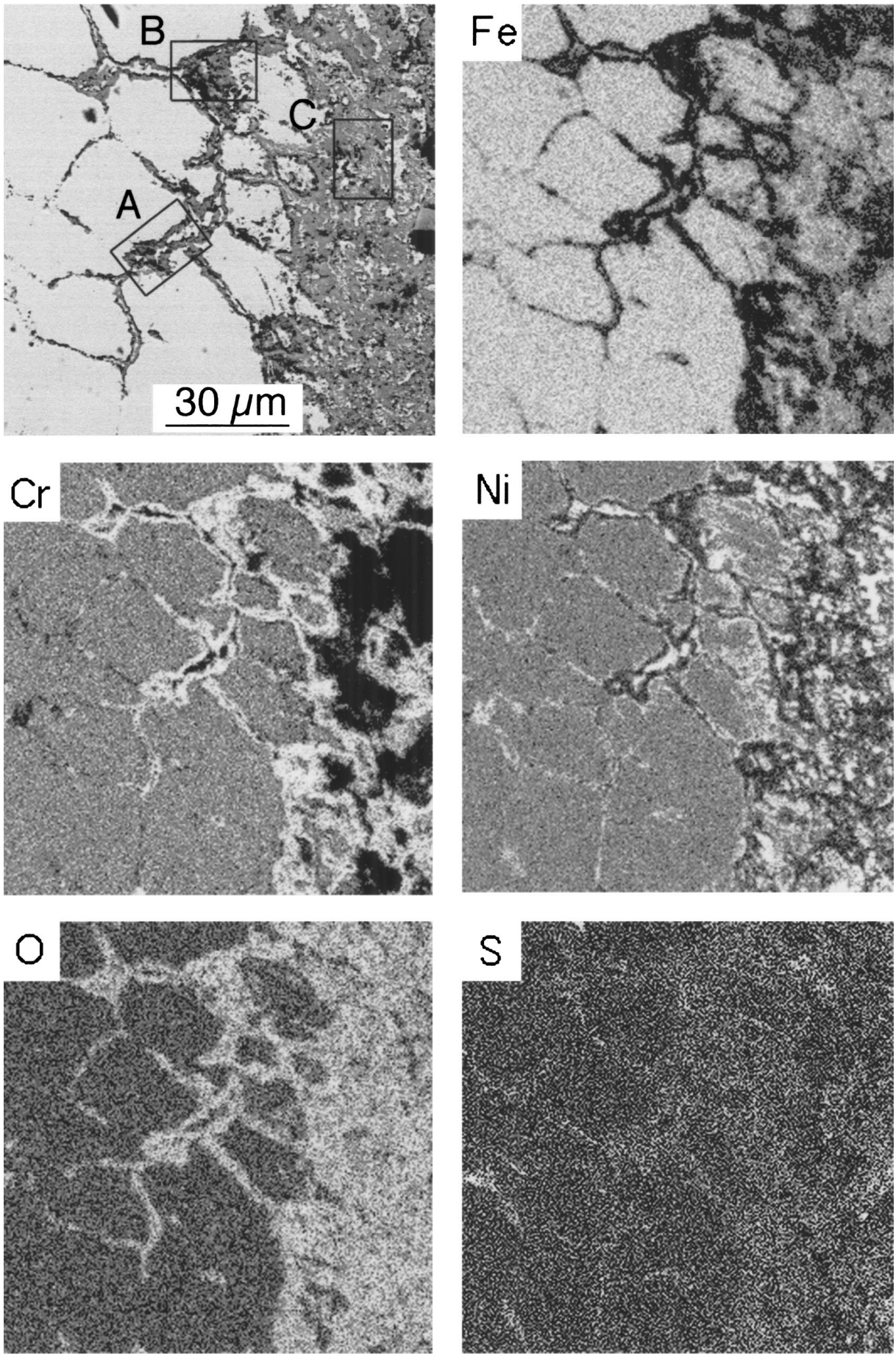

Figure 5 Elemental mapping carried out around the regions where intergranular corrosion takes place on the 600°C sample.The location is from the sample shown in Fig. 3a.

is, hence, omitted here. It seems that the intergranular corrosion is almost the exclusive result of sulphidation and independent of the strong presence of KCl in the deposit. Possible roles played by chlorination where there is a chloride or HCl (in the presence of moisture) partial pressure (Table IV) remain to be investigated.

Fig. 6 shows micrographs from the 650°C probe at similar locations to those on the 600°C probe (Fig. 3). It

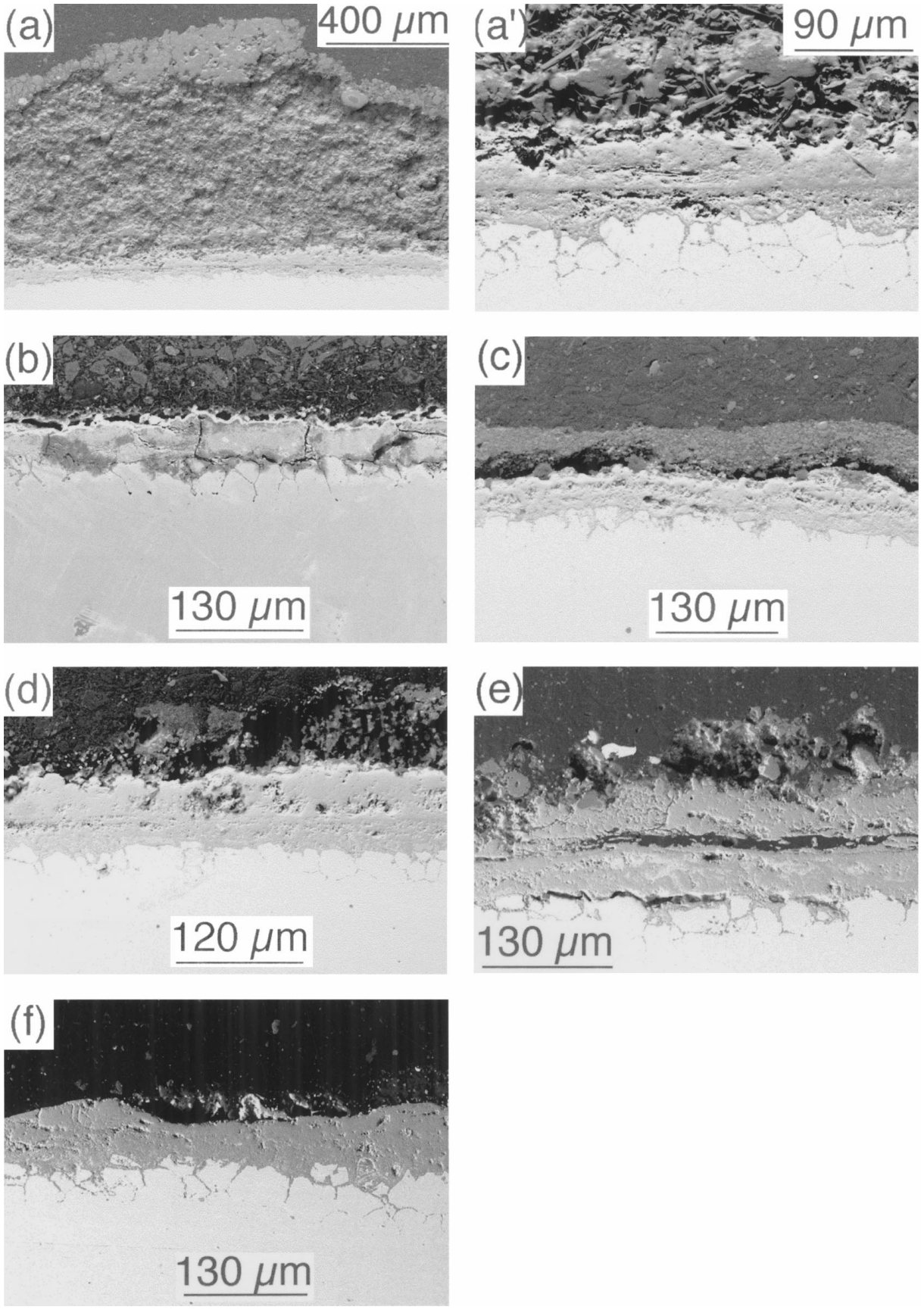

Figure 6 SEM micrographs prepared on the cross sections of the 650°C probe.The position for each photo on the probe surface is given in Fig. 3.

can be seen that the deposits on the 650°C probe appear to be more adherent, possibly because of the increased sintering at the higher temperature. Fig. 6a shows that, at the location directly facing the flue gas, a thick and dense deposit layer is formed. In particular, it seems to have a "crusted cover" on the outer surface. Fig. 6a′ is a higher magnification of this deposit/scale interface, which reveals the extent of scale growth and intergranular corrosion. It also confirms the well-sintered nature of the deposit. The enhanced sintering of the deposit on the 650°C probe is also obvious by examining micrographs from the other locations (Fig. 6c to e), as almost all show a thick ash layer. Fig. 6b comes from the location between the two types of deposits where there is almost no deposit. Comparison between Figs 3b and 6b shows that the oxidation layer (Layer 1) at 650°C is much denser and more adherent. Layer II in Fig. 6 is nearly identical to Fig. 3 and the extent of intergranular corrosion seems less. There is also very little variation between the different locations at 650°C even at the back location (Fig. 6f).

Fig. 7 shows the EDX analysis from different points of the deposit layer shown in Fig. 6a. A significant enrichment of calcium and silicon at the outer deposit (the crust) is clearly visible, and this is accompanied by marked decrease of sodium within this layer. Compared to the original fly ash composition (Table III), the Ca/K ratio is roughly the same for the crust (Point 1) but significantly less for the deposit within it (Points 2 and 3) (Table VI). This indicates that the crust is composed mainly of fly ash particles, which subsequently undergo chemical reactions themselves and with the underlying oxide scale. The overall result is that the deposit beneath the crust may be molten at operating temperatures and solidify upon cooling. Aluminium is fairly constant throughout the deposit layer. From Point 1 to 3, a slight increase of iron and sulphur is also detected which may coincide with the K_2SO_4 picked up by

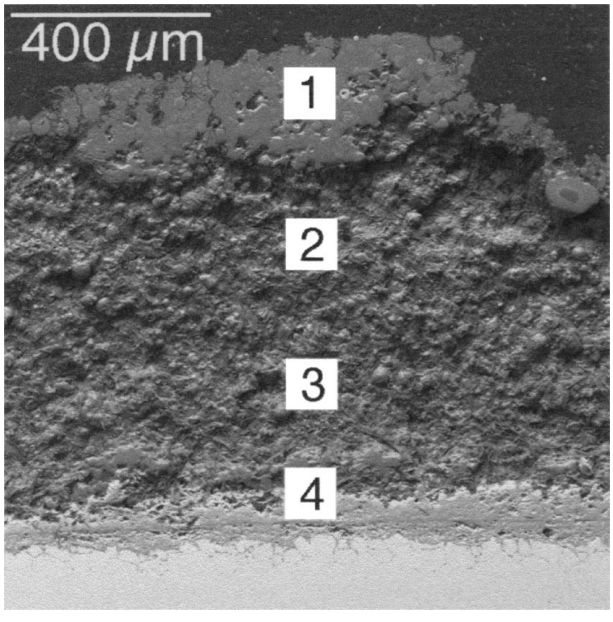

Figure 7 A cross section on the 650°C probe directly facing the flue gas and the EDX results (Table VI). Point 4 was not included in the table as the region consists of both deposit and scale.

TABLE VI EDX analysis of the deposit on the 650°C sample

Elements	The curst (Point 1)	The middle ash layer (Point 2)	The inner ash layer (Point 3)
O	25.6	33.5	36.8
Fe	0	1.6	0
Na	3.3	13.2	14.2
K	17.4	26.0	27.1
Ca	37.2	13.7	13.8
Mg	3.3	2.2	1.6
Ti	0.9	3.1	0.3
Cr	0	0.3	0.2
Mn	4.0	3.2	2.7
Ni	0	0	0
Al	1.4	1.0	1.4
Si	5.0	0.9	0.8
P	1.2	0.9	0.7
S	0.6	0.2	0.2
Cl	0.1	0.1	0.1

XRD (Fig. 2b). EDX mapping of this area was carried out and the results are shown in Fig. 8. Fig. 8 reveals the enrichment of calcium, magnesium and phosphorus at the outer crust, accompanied by a slight increase of silicon and possibly sulphur. Sodium is enriched at the deposit/metal interface. However, EDX does not reveal the presence of chloride at this cross section. Using dry grinding to minimise the loss of the deposit, Fig. 9 shows a cross section on the 650°C probe at the location of Fig. 6e together with EDX mapping of the main ash and scale elements. Comparing Fig. 9 with Fig. 8 reveals entirely different trends of the ash elements: there is no obvious preferential distribution of the ash elements in Fig. 9. Calcium, potassium and sulphur are all seen over the whole deposit. Broadly speaking, the clear presence of chloride (mainly as KCl) agrees well with the XRD results shown earlier. More specifically, it seems that that the chloride is accumulated next to the scale but hardly any within the scale. The scale consists essentially of iron oxide on top of chromium oxide. The main conclusion here is that the composition of the deposit formed on the probe ring depends on their relative location to the flue gas direction.

The results in Figs 5, 8 and 9 seem to agree with the theoretical phase stability diagrams of nickel, chromium and iron in the gaseous mixture of oxygen/sulphur and oxygen/chlorine, as shown in Fig. 10 (using 600°C as an example). In Fig. 10a, the area marked as A gives the gas partial pressures where it is thermodynamically possible to form nickel sulphide mixed with chromium oxide and iron oxide. Similarly as shown in Fig. 10b, unless a quite large chlorine partial pressure exists there would be very little possibility for the formation of chromium and iron chlorides. All these situations could represent the local environment at area A in Fig. 5, which is responsible for the initiation of intergranular corrosion. The areas B and C in both Figs 5 and 10 correspond to an increased oxygen partial pressure, therefore favouring the formation of oxides for all three elements. The outer, general corrosion layer (Layer I) sees the environment marked as D in Fig. 10 with the highest oxygen, sulphur and chlorine partial pressure and is directly in contact with molten deposit,

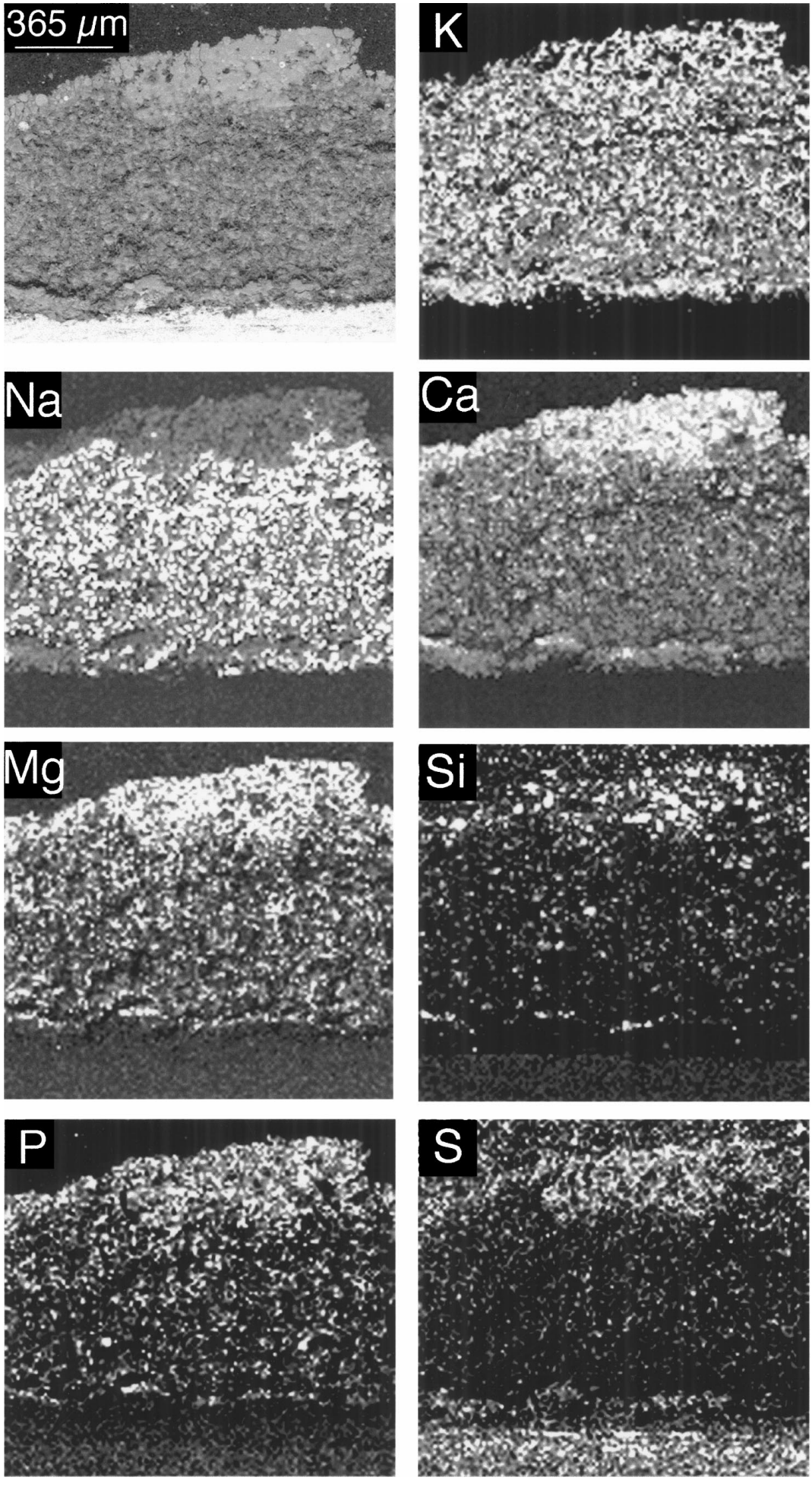

Figure 8 Elemental mapping of main ash elements across the thickness of the deposit shown in Fig. 7 formed on the 650°C probe.

which was in turn in equilibrium with the flue gas (Table IV). Therefore, fluxing reactions are most likely to dominate at these locations. A recent study by Asteman *et al.* [8] also suggests a possible link between chromium depletion at the outer general corrosion layer with the presence of moisture through the formation of volatile $CrO_2.H_2O$ gas under similar situations. Area D in both Fig. 10a and b overlaps with the CrO_2 domain,

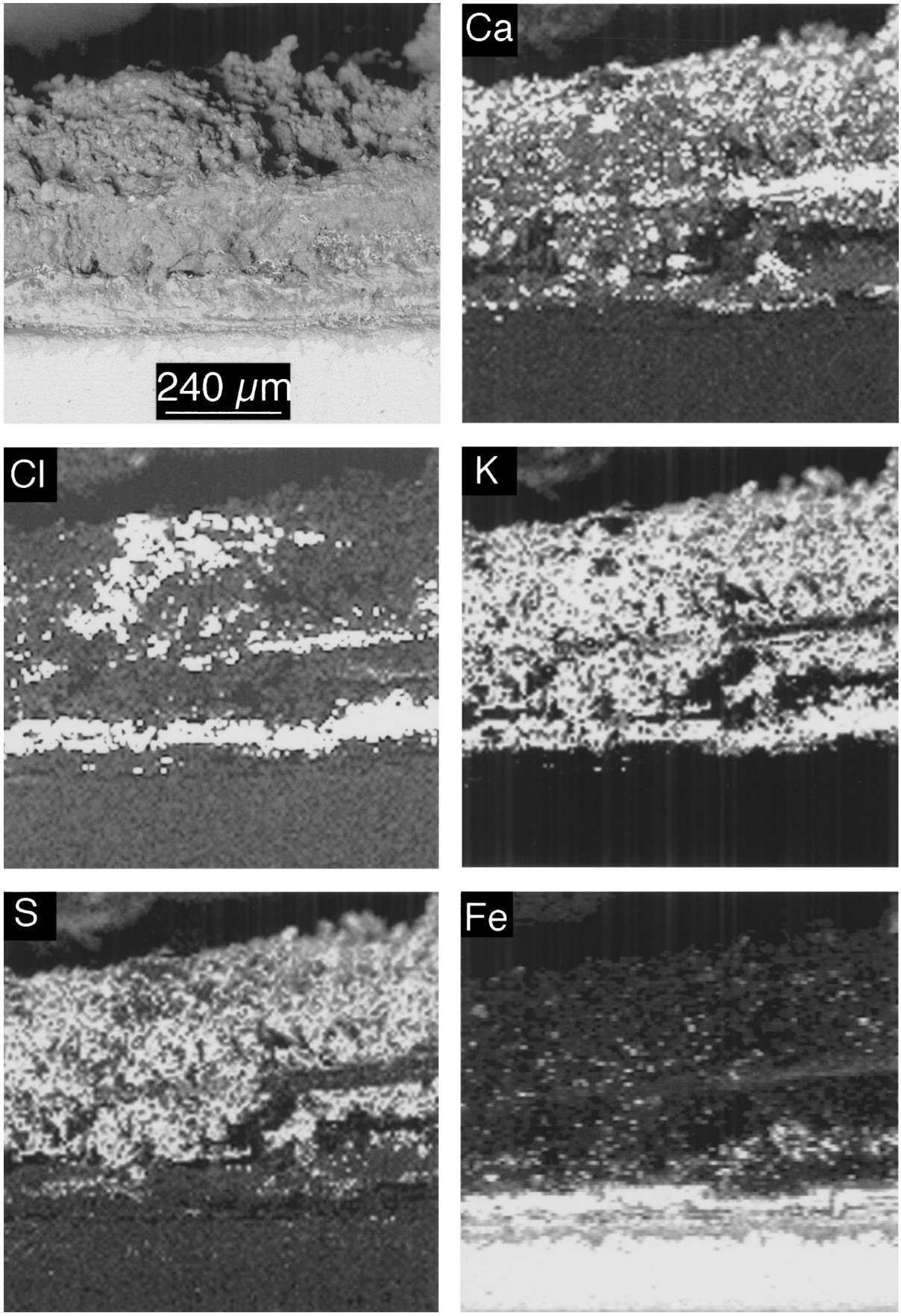

Figure 9 Elemental mapping of main ash as well as alloy elements across the deposit and the scale on the 650°C probe located roughly position Fig. 6e. (*Continued*)

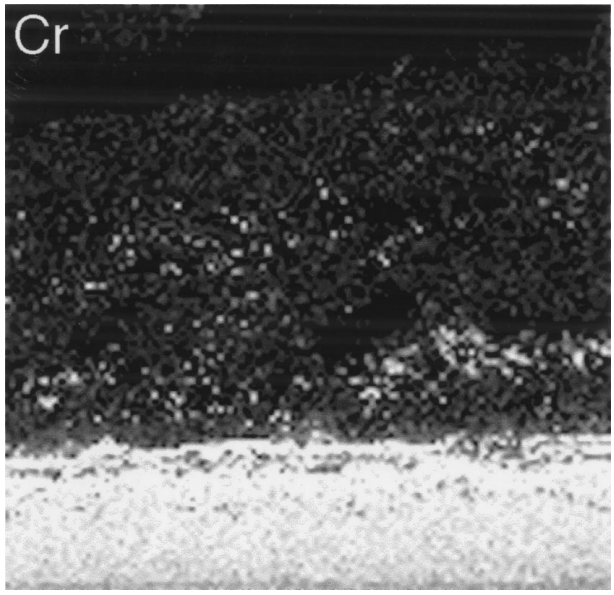

Figure 9 (*Continued*).

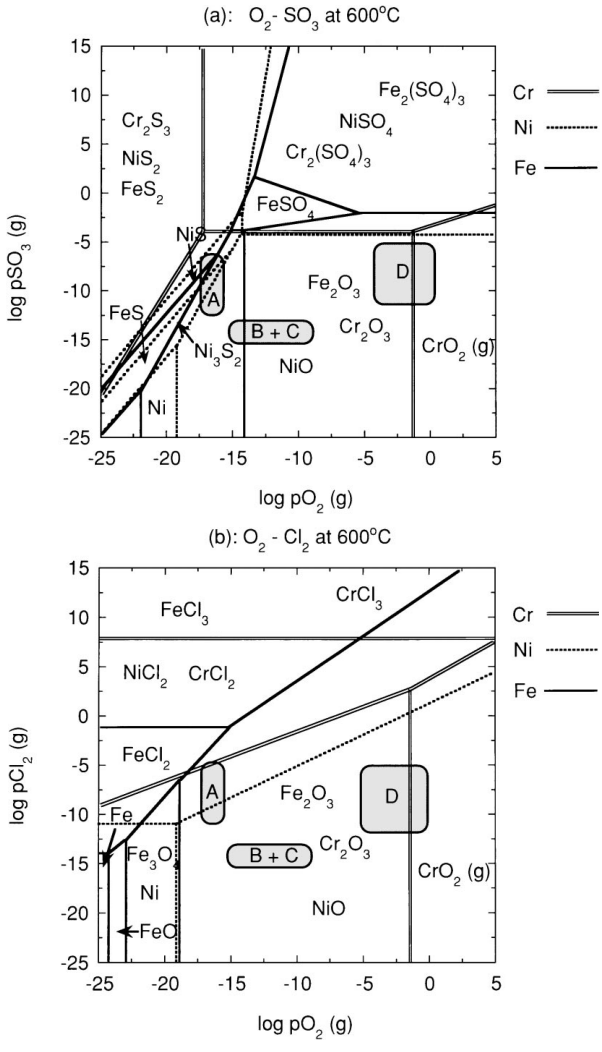

Figure 10 Theoretical phase stability diagram of nickel, chromium and iron in the gas mixture of oxygen/sulphur (a) and the oxygen/chlorine (b) at 600°C.

which itself has a theoretical melting point of 300°C, thus also confirming the possible reaction conditions at area D.

In summary, the increased temperature appears to have two major effects. Firstly, it enhances the sintering tendency of the deposits. It is very likely that this makes the deposits more "sticky" at the operating temperature, thus reflecting the aggravated problems of slagging. Secondly, oxidation of the alloy increases at the same time and this helps to develop a denser and more adherent oxide scale and thus minimise the extent of intergranular corrosion. The fact that this more protective oxide layer remains under the sintered deposits will offer enhanced corrosion protection. Despite different locations at 650°C (Fig. 6a to f), there is very little difference in the thickness of either the outer corrosion layer (Layer I) or the other two layers (Layer II and III).

3. Summary

The only variable between the two probes is the temperature. Increased temperature seems to cause a higher degree of sintering of the deposit, hence promoting slagging. The effect on the corrosion of the tube can be judged on the average material wastage over the test period (3770 h). The results suggest that increased temperature is important in determining the ash chemistry, the sintering behaviour and the alloy's ability to grow and repair its oxide layer under the deposit. These parameters will affect both the operational procedures and the service life of the tube metal. Experiments as a function of the reaction time and a wider temperature range are currently being undertaken.

As the thickness of the deposits around the tube is not constant, this may imply a variable temperature gradient across the deposit, which may influence the sintering tendency and possibly corrosion. In practice, there may also be a temperature difference between upstream side and downstream side. For laboratory hot corrosion tests utilising synthetic ashes, the observed accumulation of potassium chloride in the deposits, far exceeding the level in its original fly ash, will be very important. To simulate accurately deposit induced hot corrosion, the synthetic ash composition must contain a substantially higher amount of potassium chloride than that in the fly ash.

Acknowledgement

The authors thank the European Commission for funding this work within the framework of the Non-Nuclear Energy Programme (JOULE III) and the co-ordinator of the project at the Institute of Process Engineering and Power Plant Technology (IVD), University of Stuttgart, Germany.

References

1. B. M. JENKINS, L. L. BAXTER, T. R. MILES and T. R. (JR.) MILES, *Fuel Processing Technology* **54** (1998) 17.
2. L. L. BAXTER, *Biomass and Bioenergy* **4** (1993) 85.
3. D. C. DAYTON, R. J. FRENCH and T. A. MILNE, *Engery and Fuels* **9** (1995) 855.
4. T. R. MILES, T. R. (JR.) MILES, L. L. BAXTER, R. W. BRYERS, B. M. JENKINS and L. L. ODEN, *Biomass and Bioenergy* **10** (1996) 125.

5. F. S. PETTIT and C. S. GIGGINS, in "Superalloys II," edited by C. T. Sims, N. S. Stoloff and W. C. Hagel (John Wiley & Sons Inc., USA, 1987) p. 327.
6. Y. KAWAHARA, *Materials at High Temperatures* **14** (1996) 261.
7. J. STRINGER and I. W. WRIGHT, *Oxidation of Metals* **44** (1995) 265.
8. K. NATESAN, *JOM* **43** (1991) 61.
9. R. A. RAPP and Y. S. ZHANG, *Molten Salt Forum* **5/6** (1998) 25.
10. S. C. SRIVASTAVA, K. M. GODIWALLA and M. K. BANERJEE, *J. Mater. Sci.* **32** (1997) 835.
11. K. L. LUTHRA and D. A. SHORES, *J. Electrochem. Soc.* **127** (1980) 2202.
12. K. L. LUTHRA, *ibid.* **132** (1985) 1293.
13. W. T. REID, in "External Corrosion and Deposits: Boilers and Gas Turbines" (Elservier, New York, 1971).
14. G. Y. LAI, in "High-Temperature Corrosion of Enginnering Alloys" (ASM International, Materials Park, OH 44073, USA, 1990).
15. H. J. GRABKE, E. REESE and M. SPIEGEL, *Molten Salt Forum* **5/6** (1998) 405.
16. A. J. B. CUTLER, *Materials Science & Technology* **3** (1987) 512.
17. H. ASTEMAN, J.-E. SVENSSON, L.-G. JOHANSSON and M. NORELL, *Oxidation of Metals* **52** (1999) 95.

Received 5 October 1999
and accepted 5 April 2000